

Tailoring Emergent Magnetic Moment in $\text{La}_{0.7}\text{Sr}_{0.3}\text{MnO}_3\text{-Bi}_2\text{Te}_3$ Heterostructures *via* Interfacial Reconstructions

Damian Brzozowski,¹ Yu Liu,¹ Øyvind Finnseth,¹ Egil Y. Tokle,¹ Andrew J. Caruana,² Christy J. Kinane,² Alexander J. Grutter,³ Dennis G. Meier,^{1,4} and Ingrid G. Hallsteinsen^{1,*}

¹*Department of Materials Science and Engineering,
Norwegian University of Science and Technology, Trondheim, Norway*

²*ISIS Facility, STFC Rutherford Appleton Laboratory,*

Harwell Science and Innovation Campus, Didcot, Oxfordshire, United Kingdom

³*NIST Center for Neutron Research, National Institute of Standards and Technology, Gaithersburg, Maryland, United States*

⁴*Faculty of Physics, University of Duisburg-Essen, Germany*

We report emergent magnetic behavior in heterostructures composed of (111)-oriented $\text{La}_{0.7}\text{Sr}_{0.3}\text{MnO}_3$ (LSMO) and (00 l)-oriented Bi_2Te_3 (BT), controlled by interfacial reconstructions. When BT is deposited directly onto LSMO, an intermediate interfacial layer forms between the two materials. Polarized Neutron Reflectometry modeling reveals that this reconstructed region stabilizes a secondary magnetically ordered phase that is coupled to the underlying ferromagnetic LSMO layer. As a consequence, the heterostructures exhibit unconventional self-crossing magnetic hysteresis loops at room temperature, characterized by a reversal of the net magnetization at low applied fields. In contrast, the introduction of a tellurium seed layer results in a sharper LSMO-BT interface, while preserving the anomalous hysteresis behavior and enhancing the saturation magnetization. Element-specific X-ray absorption spectroscopy suggests that the emergent magnetic phase originates from the chemical reconstruction of manganese species. These results demonstrate that interface engineering in magnetic oxide-topological insulator heterostructures provides a pathway to control emergent magnetic coupling and emergent magnetic states in oxide-topological insulator heterostructures.

Emergent functional properties in material systems have attracted considerable interest for advanced electronic and spintronic applications [1–3]. By combining materials with distinct physical characteristics in the form of heterostructure systems, it is possible to enable physical phenomena that cannot be realized in individual constituents alone. In particular, interfaces between materials with dissimilar crystal structures often host novel electronic and magnetic states arising from interfacial reconstruction and symmetry breaking. Such heterostructures have enabled a range of emergent interfacial phenomena, including interfacial superconductivity, controllable Rashba spin-orbit coupling, and axion insulating states [4–6].

A major objective is the realization of robust topological transport at elevated temperatures in magnetic topological insulators (TIs), where the interplay between magnetic order and electronic band topology can produce chiral surface conduction channels [7–10]. In the Quantum Anomalous Hall Effect (QAHE), time-reversal symmetry breaking opens an exchange gap in the Dirac surface states, enabling dissipationless edge transport. In practice, however, the temperature at which quantized Hall transport is observed is typically far below both the predicted exchange and the magnetic ordering temperature of the system. This discrepancy arises because the QAHE is highly sensitive to spatial inhomogeneities. Variations in magnetic exchange coupling, fluctuations of the chemical potential, and parasitic bulk or defect conduction channels can all reduce the effective gap controlling quantized transport.

Several approaches have been explored to introduce magnetism into TIs. One widely used strategy involves doping TI chalcogenides with magnetic elements such as V, Cr, or Mn, which has enabled observation of the QAHE at temperatures below a few kelvin [7, 11–13]. Alternatively, intrinsically magnetic topological insulators such as MnBi_2Te_4 host magnetic order within the topological material itself [14–17]. However, both approaches suffer from disorder associated with dopant incorporation or structural defects, which can produce spatial fluctuations in the magnetic gap and chemical potential, ultimately suppressing robust quantized transport. An alternative route relies on the magnetic proximity effect (MPE), in which a TI is interfaced with a magnetically ordered material [18–22]. In principle, this approach avoids dopant-induced disorder and enables the use of magnetic materials with high Curie temperatures. In practice, however, realizing strong proximity coupling requires sharp interfaces, low defect densities, and minimal interfacial intermixing. Atomic reconstruction, diffusion, or the formation of intermediate phases can strongly modify the electronic structure at the interface and lead to spatially nonuniform magnetic coupling [23]. So far, the highest temperature reported for the QAHE in interfacial systems is approximately 0.1 K, far below the magnetic ordering temperatures of the constituent layer [24].

In this letter, we examine the FM-TI heterostructures composed of (111)-oriented $\text{La}_{0.7}\text{Sr}_{0.3}\text{MnO}_3$ (LSMO) and (00 l)-oriented Bi_2Te_3 (BT). LSMO is a ferromagnetic half-metal oxide perovskite with a high Curie temper-

ature, widely studied for its strong correlated electron behavior [25, 26] and colossal magnetoresistance [27–29], while BT is a prototypical model three-dimensional topological insulator [30, 31]. Perovskite–chalcogenide FM–TI heterostructures remain largely unexplored. However, several experimental [21, 32–37] and theoretical [34, 36, 38] reports were presented, including LSMO-based FM–chalcogenide heterostructures [35, 38]. Achieving high-quality interfaces between oxide perovskites and chalcogenide TIs is challenging due to structural and chemical incompatibilities. To address this, we employ two growth approaches: direct deposition of BT onto LSMO, and growth mediated by a tellurium seed layer. The seed layer promotes ordered crystalline nucleation, passivates the surface and acts as a tellurium reservoir during BT growth, thereby reducing interfacial roughness and suppressing the formation of intermediate phases.

The crystalline quality of the samples fabricated is characterized using X-ray diffractometry. Magnetic properties were investigated using bulk magnetometry measurements, as well as element-resolved X-ray absorption spectroscopy and depth-sensitive Polarized Neutron Reflectometry. Depth-resolved magnetic profiles obtained from modeling specular Polarized Neutron Reflectometry data indicate the formation of an intermediate layer between LSMO and BT when the direct-growth approach is employed. In contrast, the data for the seed-layer sample are successively modeled without the need of implementing secondary phases into the stack. In either case, an induced magnetic ordering arises. Magnetic dichroism measurements help determine the contribution of manganese and tellurium species to the interfacial reconstructions and emergent magnetism. Magnetometry measurements reveal unconventional magnetic behavior that is dependent on temperature, FM layer thickness, and the use of seed layers. It is reflected in the formation of self-crossing hysteresis loops and loop shifting along the applied field axis. We further compare these results with a single LSMO thin film and demonstrate that by tuning the thickness of the LSMO layer in LSMO–BT heterostructures, the bulk magnetic response can be modified. By integrating high-temperature FM order with TI layers, this work advances the understanding of magnetic coupling in FM–TI heterostructures and provides design guidelines for robust hybrid heterostructures in future electronic and spintronic applications.

EXPERIMENTAL

LSMO–BT samples were prepared on (111)-oriented SrTiO₃ (STO) substrates (Shinkosha) *via* Pulsed Laser Deposition (PLD) using the direct growth approach and the seed-layer approach with tellurium deposited before the growth of BT. The substrates were cleaned in a son-

ication bath of acetone, ethanol, and deionized water for 5 minutes each. The cleaning procedure was followed by etching in a buffered hydrofluoric acid solution (1:9 ratio of HF and NH₄F) for 45 seconds to achieve single termination of the surface. To ensure a smooth step-terrace topography, the substrates were annealed at 1050 °C for 1 hour in O₂ flow.

The substrates were cleaned in an ethanol sonication bath for 3 minutes prior to installation on a PLD holder inside the chamber, and subsequently degassed through the annealing process at 400 °C for 1 hour at a base pressure of $\sim 5 \times 10^{-8}$ mbar. A KrF excimer laser ($\lambda = 248$ nm) was used to deposit all layers. For La_{0.7}Sr_{0.3}MnO₃, the laser was set to the pulsing frequency $\nu = 1$ Hz and laser fluence $f = 2.0$ J cm⁻². Target to substrate distance $d_{ts} = 50$ mm. The substrate temperature T was monitored with a pyrometer and set at 650 °C. O₂ gas was introduced into the chamber for the deposition pressure $p = 0.3$ mbar. Post-deposition annealing was performed at 100 mbar O₂ for 1 hour to minimize oxygen vacancies. Growth conditions of Bi₂Te₃ were set as follows: temperature $T = 220$ °C, pressure $p = 1.0$ mbar Ar, target to substrate distance $d_{ts} = 45$ mm, laser pulsing frequency $\nu = 0.2$ Hz and fluence $f = 0.5$ J cm⁻². For the seed-layer sample, a thin tellurium film was deposited prior to the deposition of Bi₂Te₃. Tellurium was deposited at room temperature, at a base pressure of $\sim 5 \times 10^{-8}$ mbar, distance $d_{ts} = 50$ mm, frequency $\nu = 1$ Hz, and fluence $f = 1.5$ J cm⁻².

High-resolution X-ray diffraction (HRXRD) was employed for thickness estimation of each layer. Additionally, reciprocal space mapping was performed around (123)STO peak to assess the lattice straining of LSMO. Both HRXRD and RSM scans were carried out using the D8 Discover diffractometer equipped with a 2-bounce Ge (220) monochromator and Cu K_α radiation ($\lambda = 1.5406$ Å). The HRXRD data of the oxide layers were fitted using the InteractiveXRDFit MATLAB package [39].

Depth-resolved Polarized Neutron Reflectometry (PNR) measurements were conducted on thick heterostructures at the PolRef beamline of the ISIS Neutron and Muon Source (Didcot, UK). The measurements were taken at 300 K, under an applied in-plane field of 0.7 T. Open-source *Refl1D* fitting software package was used to build a matching sample model and obtain nuclear and magnetic scattering length density profiles. The considered PNR models were consequently expanded, starting from the simplest stack, and based on the previously collected structural and magnetic data. The final models are discussed in the paper, and the full modeling methodology is presented in detail in the Supporting Information.

Element-resolved X-ray Magnetic Circular Dichroism (XMCD) measurements were performed on manganese

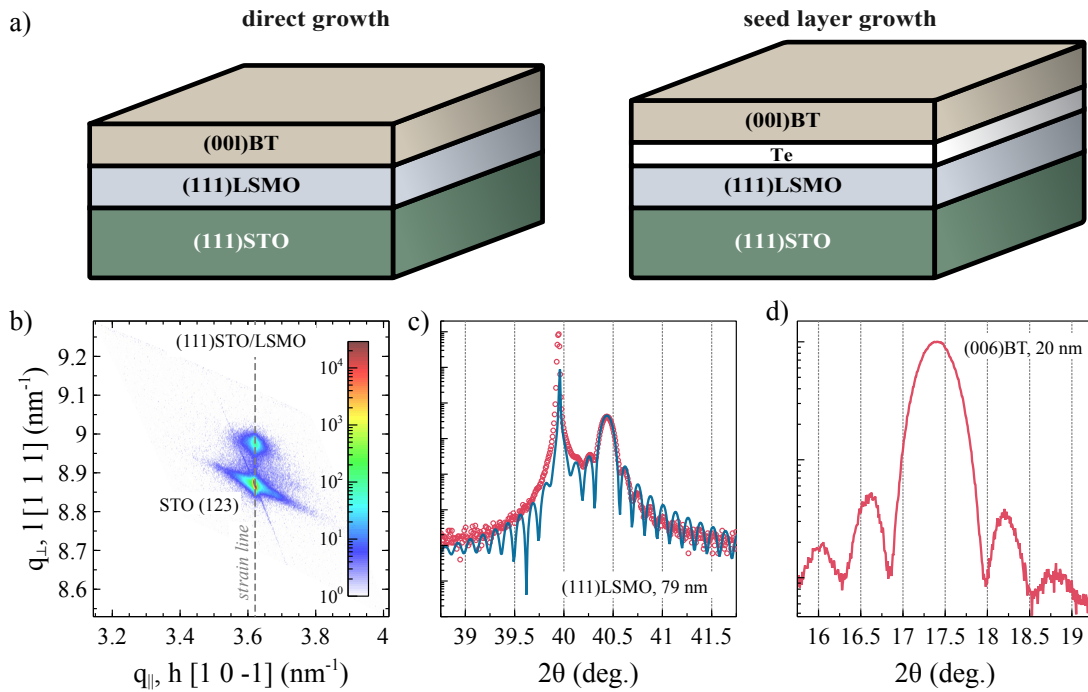


FIG. 1. a) Schematic illustration of the LSMO-BT heterostructures discussed. One stack is grown with a direct contact between LSMO and BT layers (left), whereas the other has an additional tellurium seed layer deposited prior to the growth of the BT layer (right). b) RSM of (111)-LSMO around asymmetrical (123)⁺ peak of STO. The RSM confirms the epitaxial relation between the film and the substrate, showing that LSMO thin film grows under tensile strain on STO. c) HRXRD of (111)-LSMO film deposited onto (111)-STO. The thickness is estimated using the InteractiveXRDFit package. d) HRXRD of (006)-Bi₂Te₃ with Te seed layer and estimated 20 nm thick layer.

L edges and tellurium M edges to confirm the origin of ferromagnetic ordering. The measurements on Mn L_{3,2} edges were performed at the beamline BL-16A of Photon Factory (Tsukuba, Japan), and the measurements on Te M_{5,4} edges were carried out at the beamline I10-1 of Diamond Light Source (Didcot, UK). The data presented were collected using the total electron yield (TEY) mode. An incidence angle was set at 30° relative to the surface. The magnetic field $H = 0.7$ T was applied parallel to the X-ray beam. The plotted spectroscopy profiles were divided by the I_0 beam channel. This is particularly important for the tellurium profiles, as the optics of the beamlines contain chromium, whose L_{3,2} edges are located in close vicinity to tellurium's probed M_{5,4} edges. All profiles were then normalized to the nearest peak's maximum.

A series of magnetometry measurements was performed to characterize the net magnetic behavior of the samples. Because the samples were grown with larger lateral dimensions (10×10 mm²) for PNR measurements, they could not be accommodated in the standard magnetometer sample holder. Therefore, magnetization measurements were performed after the completion of the PNR experiment, after the samples were cut to the appropriate dimensions. The measurements were performed using the Quantum Design Physical Property

Measurements System (PPMS) with the Vibrating Sample Magnetometer (VSM) mode. For comparison, additional field-dependent magnetization curves were collected on the single LSMO thin film and an LSMO-BT heterostructure with the thinner LSMO layer using the Superconducting Quantum Interference Device (SQUID) MPMS magnetometer. Prior to each measurement, samples were warmed above their Curie temperature T_C , demagnetized using the oscillation mode, and cooled to the target temperature for field-dependent magnetization measurements. Each loop was acquired in the field range of ±0.5 T.

RESULTS

LSMO and BT belong to different crystal systems, rendering high-quality interfaces particularly challenging to achieve. Several reports show the formation of amorphous phases at the interface, which is known to alter the coupling between the materials. One strategy to control the morphology at the interface is to deposit a seed layer prior to Bi₂Te₃ deposition, which has been shown to passivate the surface and suppress atomic intermixing. In addition, the tellurium seed layer acts as a tellurium reservoir for newly formed BT layers, minimizing

point defects and preserving the 2:3 atomic stoichiometry. With this in mind, two LSMO-BT heterostructures were grown as schematically depicted in Figure 1(a)-one with the direct growth, and the other with the seed layer. In order to confirm a high-quality growth of LSMO, RSM is collected around the $(123)^+$ peak of STO. Figure 1(b) shows the data collected for the first sample. The RSM is plotted in the scattering vector space, where q_{\parallel} denotes the in-plane component, and q_{\perp} the out-of-plane component. The "+" superscript denotes the grazing exit geometry, which in contrast to the grazing incidence geometry probes deeper into the thin film and is more sensitive to structural changes in the bulk of the film. STO and LSMO peaks reside at the same q_{\parallel} vertical line at 3.62 nm^{-1} , confirming that LSMO film is in tensile strain upon growth on (111)-STO. For a relaxed (111)-LSMO film with the pseudocubic lattice constant $a_{pc} = 3.87 \text{ \AA}$, the (123) peak resides at $q_{\parallel} = 3.65 \text{ nm}^{-1}$. This q_{\parallel} shift then corresponds to the lattice mismatch of -0.9%, in agreement with the expected value. The LSMO peak does not display signs of film relaxation – an otherwise relaxed film would manifest through the peak with a weak intensity tail drifting towards higher q_{\parallel} values. Figure 1(c) depicts high-resolution X-ray diffractograms of the first sample. The corresponding data for the second sample is provided in Supporting Information. The data is fit with the InteractiveXRDFit package. The fitting yields an LSMO epilayer with the thickness of 78.89 nm for the sample with direct growth, and 74.55 nm for the seed-layer sample. Lastly, Figure 1(d) shows HRXRD of the (006) peak of BT. The presence of lattice fringes confirms well-defined out-of-plane stacking. From the Bragg's law, the thickness of the BT layer is estimated to be about 20 nm. Thickness calculations are further utilized to construct PNR models.

Polarized Neutron Reflectometry

To provide a nuanced view of the structural-magnetic coupling in the LSMO-BT system, it is critical to address the following questions. Firstly, the influence of Te seed layer on the formation of intermediate amorphous phases must be evaluated. Secondly, a depth-resolved magnetization profile of a sample must be determined to understand whether an emergent magnetic ordering is accommodated at other layers than LSMO. To this end, we performed comparative Polarized Neutron Reflectometry measurements on both samples. The measurements were collected at 300 K and 110 K – slightly above the phase transition temperature of STO $T \approx 105 \text{ K}$, below which the structure of STO becomes tetragonal. PNR measures the reflected intensity of a spin-polarized neutron beam incident on the sample surface at a grazing angle. It is sensitive to the nuclear (ρ_N) and magnetic (ρ_M) scattering length density depth profiles of the sam-

ple, which are determined by the composition/density and net in-plane magnetization, respectively. By fitting the spin-dependent reflectivities as a function of the momentum transfer vector along the normal direction of the film, the depth profiles ρ_N and ρ_M may be reconstructed.

In addition to spin-dependent neutron reflectivities, it is often instructive to view the spin asymmetry, defined as $SA = (R^{++} - R^{--}) / (R^{++} + R^{--})$, which emphasizes the magnetic contributions to the scattering. Figure 2 shows the intensity of the reflected beam R , spin asymmetry SA , and the nuclear/magnetic scattering length density profiles (ρ_N and ρ_M) constructed based on the model fitting using the *Refl1D* software. The detailed modeling protocol is presented in the Supporting Information, where fitting models are built step-by-step from the simplest stack expected. The summary of the sample stacks is shown in Table I.

First, the results of the direct-growth heterostructure are discussed as shown in Figure 2(a). The optimal fit reaches the figure of merit $\chi^2 = 1.93$. It estimates that the thickness of the LSMO layer is $72.9 \pm 2.1 \text{ nm}$, which deviates from the HRXRD fit by approximately -6.0 nm. The roughness at the interface between LSMO and the following layer is $9.0 \pm 1.0 \text{ nm}$ at 300 K and $8.7 \pm 1.1 \text{ nm}$ at 110 K. An important feature emerges above the LSMO layer, where an interfacial layer is introduced before BT. The estimated thickness of this layer is about $10.2 \pm 2.0 \text{ nm}$. The BT layer has a thickness of $15.4 \pm 0.9 \text{ nm}$, and is followed by a subsequent oxidized BT, with a thickness of $4.7 \pm 1.3 \text{ nm}$. The sum of the thicknesses of the pristine and oxidized BT layers results in a close match to the HRXRD data. The topmost layer named *surface* refers to various contaminants (commonly hydrocarbon compounds) accumulated on the surface of the samples, which affect the reflectivity decay. Critically, the model predicts that the magnetic moment extends beyond LSMO and reaches both the interfacial layer and the BT layer. The ρ_N values achieved at both temperatures are summarized in Table I. The magnetization at the interface is enhanced with respect to the magnetization of LSMO, which may indicate that manganese species diffuse and accumulate at this layer. It is important to emphasize that alternative models with the fixed zero ρ_N at the interface and BT resulted in less optimal fits. The model constructed for the seed-layer sample shown in Figure 2(b) yields the figure of merit $\chi^2 = 1.56$ without the interfacial layer and is the most optimal fit achieved for this sample. The other models tested include the introduction of magnetic and non-magnetic interfacial layers, as well as the separate tellurium layers. The model shows that the sample hosts the magnetization higher than the direct-growth heterostructure. Moreover, the magnetization persists within the BT layer, suggesting a partial incorporation of magnetic species within the BT layer or emergent magnetization through the proximity effect.

TABLE I. Summary of PNR fitting parameters for LSMO-BT heterostructures with the direct growth and seed layer. The samples are split into the corresponding constituents (stack layers), and the thickness and the nuclear/magnetic SLD values are presented. For mSLD, both 300 K and 110 K values are provided in the top and the bottom rows, respectively

stack	direct growth			seed layer		
	d (nm)	ρ_N (10^{-4} nm $^{-2}$)	ρ_M (10^{-4} nm $^{-2}$)	d (nm)	ρ_N (10^{-4} nm $^{-2}$)	ρ_M (10^{-4} nm $^{-2}$)
<i>surface</i>	11.5 ± 1.3	1.03 ± 0.16	0.00	9.2 ± 1.0	1.50 ± 0.10	0.00
<i>oxidized BT</i>	4.7 ± 1.3	2.95 ± 0.46	0.00	5.3 ± 1.4	3.15 ± 0.54	0.00
<i>BT</i>	15.4 ± 0.9	1.73 ± 0.09	0.06 ± 0.04 0.44 ± 0.06	11.0 ± 1.2	2.19 ± 0.02	0.16 ± 0.18 0.43 ± 0.20
<i>interface</i>	10.2 ± 2.0	3.02 ± 0.16	0.85 ± 0.09 1.61 ± 0.11	–	–	–
<i>LSMO_{top}</i>	–	–	–	$69.0 \pm$	3.71 ± 0.03	1.01 ± 0.02 1.53 ± 0.02
<i>LSMO_{bottom}</i>	72.9 ± 2.1	3.81 ± 0.02	0.69 ± 0.03 1.35 ± 0.02	$11.9 \pm$	4.03 ± 0.07	1.01 ± 0.02 1.53 ± 0.02

These two mechanisms cannot be distinguished unambiguously from PNR alone. In addition to the absence of an intermediate layer, the roughness of LSMO with the neighboring layer is decreased and equals 5.4 ± 0.4 nm at 300 K and 4.4 ± 0.3 nm at 110 K. The interpretation of the PNR data is that in both the case of the direct growth and the seed layer growth there is a spatially extended magnetization outside of LSMO, and that the seed layer approach provides a more uniform interface between LSMO and BT.

X-ray Magnetic Circular Dichroism

The emergence of an intermediate layer between LSMO and BT raises the question of what is the element-specific origin of the stabilized phase and the magnetic ordering. The most likely contributors would be manganese acting as the magnetic reservoir and tellurium as it is highly prone to the desorption and diffusion effects, resulting in Te-deficient BT. Interfacial reconstructions are expected to alter the valency of contributing elements and therefore it is likely that the change can be observed with X-ray absorption spectroscopy. For this reason, XAS and XMCD measurements were carried out on the direct-growth heterostructure. The Mn $L_{3,2}$ edges of LSMO are well-explained in the literature, and generally yield a high signal-to-noise ratio. To compare the Mn edges of the LSMO-BT heterostructure with unaltered Mn edges of a single LSMO layer, comparative analysis is performed and presented in Figure 3. Figure 3(a) shows the absorption spectra of Mn $L_{3,2}$ edges of the direct-growth heterostructure. The L_3 and L_2 edges correspond to the $2p_{3/2} \rightarrow 3d$ and $2p_{1/2} \rightarrow 3d$ excitations, respectively. Subscripts *A* and *B* refer to excitations to the $3d e_g$ and $3d t_{2g}$ bands, respectively. The dichroism curve confirms the FM ordering of manganese within the sample, and reaches 42% at photon energy of 640.4 eV. Figure 3(b) compares the XAS of the direct-growth heterostructure and a single LSMO film. The

LSMO curve (red line) is in agreement with other reports on the Mn $^{3,3+}$ valence state [40, 41]. The heterostructure curve (blue line) deviates from that of a single LSMO layer. An increased intensity is observed at $E = 638$ eV and 649 eV, marked with arrows, matching the energy of excitations to the Mn $3d t_{2g}$ orbitals. Alternatively, the change may be from a contribution from a lower oxidation state, e.g., Mn $^{2+}$. The intensity on the high-energy-side is increased, as well. The comparison suggests that manganese may diffuse from the LSMO layer to the intermediate layer, where it stabilizes a phase over an altered oxidation state. This scenario is reinforced under the consideration that the PNR modeling magnetizes the interfacial region.

Unlike manganese, whose $L_{3,2}$ edges yield a robust signal, the tellurium $M_{5,4}$ edges have a weak intensity relative to the background level. In addition, many X-ray magnetic dichroism beamlines employ chromium optics along the pathway, whose $L_{3,2}$ edges lie closely to the tellurium M edges. These challenges make the dichroism analysis of tellurium particularly difficult. Nevertheless, several reports successfully present magnetic dichroism on tellurium edges due to magnetic proximity effects. In order to examine the contribution of tellurium to the interfacial magnetic state, XAS and XMCD are taken on the $M_{5,4}$ edges of the direct-growth heterostructure as shown in Figure 4. Figure 4(a) displays two regions of interest: the M_5 edge of the $3d_{5/2} \rightarrow 5p$ excitation, and the M_4 edge of the $3d_{3/2} \rightarrow 5p$ excitation. Each region consists of two distinct features numbered at the bottom of the figure and marked with dashed lines, located at 571.2 eV (1) and 575.1 eV (2) for M_5 , as well as 582.1 eV (3) and 585.3 eV (4) for M_4 . The peak located at 571.2 eV and the broad feature 582.1 eV (lines 1 and 3) match the tellurium oxidation state expected in Bi_2Te_3 . The features at 575.1 eV and 585.3 eV (lines 2 and 4) resemble those originating from the Te^{4+} states present in oxidized tellurium layers such as TeO_2 . Considering that the spectra are acquired in the TEY mode, which is a surface sensitive technique, it is likely that both the sur-

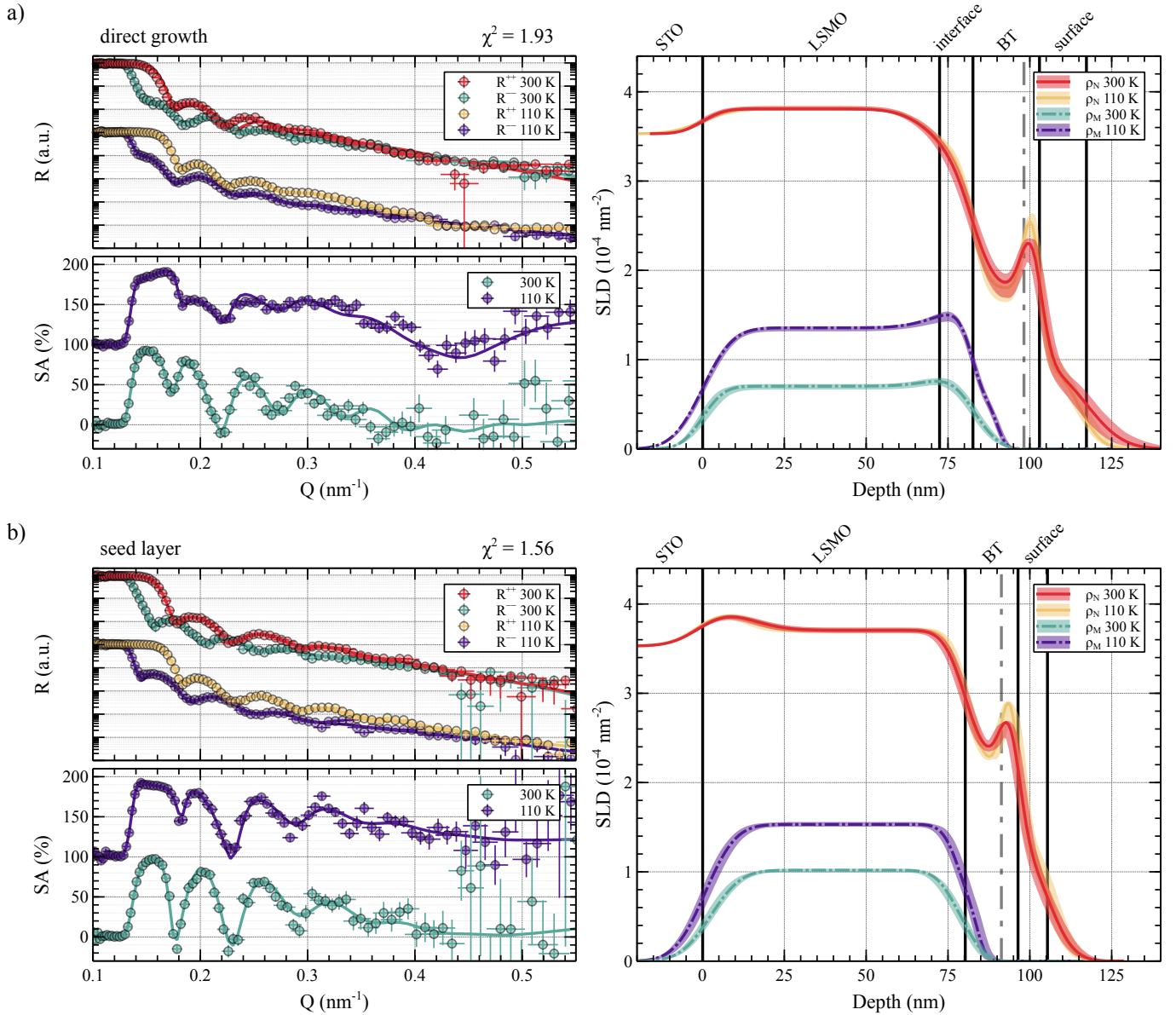


FIG. 2. PNR data (reflectivity R and calculated spin asymmetry SA) and ρ_N/ρ_M profiles of LSMO-BT heterostructures grown using the direct growth (a) and the Te seed layer (b) approach. The data was collected at $T = 300$ K and 110 K. The 300 K data is shifted along the y -axis for clarity. The shaded areas on the SLD profiles mark the 95% Bayesian confidence intervals. The dashed gray lines indicate the boundary between the pristine and the oxidized BT layers. The achieved figure of merit χ^2 values are written above the plots. For the direct growth sample, the *Refl1D* fit of $\chi^2 = 1.93$ predicts formation of an intermediate interfacial phase with induced magnetic moment. For the seed layer sample, the fit of $\chi^2 = 1.56$ is achieved without the interfacial layer and with induced magnetic moment within the BT layer.

face oxidized states and pristine Bi_2Te_3 states are probed at the same time. In addition, it is possible that a weak contribution from chromium, present in the beamline's optics, is seen at 576 eV despite dividing the signal by the total beam intensity I_0 .

Figure 4(b) shows the corresponding dichroism curve (green line). At energies corresponding to M_5 peaks, there is the dichroism of 5%. The dichroism at the peak located at 585.3 eV (M_4 edge, line 4) reaches up to 10%.

It must be taken into account that the observed XMCD signal may arise due to artifacts and overall weak signal of the tellurium M edges. Importantly, the measurement taken with the reversed magnetic field (purple line) does not lead to signal inversion at 571.2 eV (1) and 585.3 eV (4), putting in doubt the magnetic contribution of tellurium at these edges. The dichroism at 575.1 eV exhibits sign reversal of about the same magnitude, which may indicate magnetic ordering in the oxidized tellurium

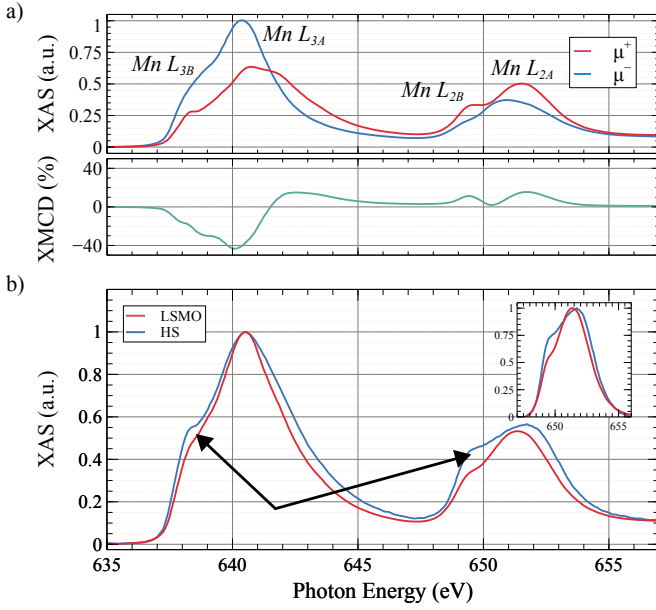


FIG. 3. X-ray absorption and dichroism spectra of the Mn $L_{3,2}$ edge. a) XAS and XMCD of the heterostructure with the direct growth. The dichroism intensity is expressed as a fraction of the XAS signal, normalized to the edge's maximum. b) Comparative XAS of the direct-growth heterostructure and a single LSMO thin film. The plot inset shows the Mn L_2 edge.

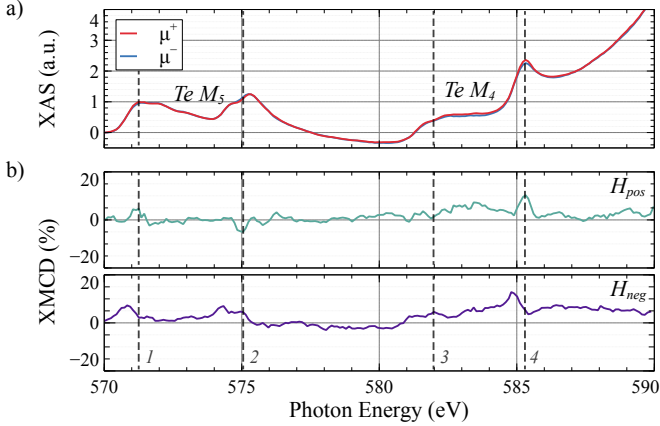


FIG. 4. a) X-ray absorption spectra of the Te $M_{5,4}$. b) The corresponding dichroism spectra (green line) and the dichroism spectra collected upon the magnetic field reversal (purple line).

phase. However, considering the weak signal of the edges probed, this observation is not conclusive. Conversely, the lack of dichroic effect at tellurium edges does not imply an absence of the magnetic proximity effect. In studies on Bi_2Te_3 films interfaced with magnetic layers, the anomalous Hall effect was observed through transport measurements despite no XMCD on the Te M edges. This can be a result of weak bonding between TI and FM, which leads to only a weak transfer of the magnetic ex-

change. As calculated, the band gap opening of 10 meV led only to a difference of about 1.6%, which lies below the detection limit in our case.

Bulk Magnetometry

Lastly, to evaluate whether interfacial magnetic reconstructions produce a measurable impact on the macroscopic net magnetization, magnetometry measurements were performed. In general, bulk magnetometry techniques such as VSM and SQUID exhibit limited sensitivity to weak induced magnetic moments, such as those associated with magnetic topological insulating phases. Nevertheless, several previous studies have reported modifications in hysteresis behavior and enhanced magnetic responses, as evidenced by $M(H)$ and $M(T)$ measurements.

Figure 5(a) presents $M(H)$ hysteresis loops for the direct growth and seed-layer heterostructures, measured at $T = 300$ K and 110 K. The data are magnified near zero field to emphasize low-field features, while full sweep loops are provided in the Supporting Information. At room temperature (red lines), both samples exhibit self-crossing hysteresis loops. Arrows indicate the direction of the magnetic field sweep for individual curves. At high applied fields, the response is characteristic of a conventional ferromagnet, with the magnetization approaching saturation. The normalized saturation magnetization at $T = 300$ K is $1.34 \mu_B/\text{Mn}$ for the direct growth sample. For the seed-layer sample, the saturation magnetization is enhanced and equals $1.85 \mu_B/\text{Mn}$.

As the applied field decreases to approximately 10-20 Oe, a pronounced reduction in magnetization occurs, and the magnetic moment reverses direction before the applied field reaches zero. Upon increasing the field in the opposite direction, the magnetization recovers its saturation value. The magnetization reversal process is reproducible in the reverse sweep. Notably, the hysteresis loops are shifted along the applied field axis by approximately -1.7 Oe and -1.9 Oe for the direct growth and seed-layer samples, respectively. No detectable shift is observed along the magnetization axis.

In contrast, the hysteresis loops measured at $T = 110$ K (blue lines) do not display self-crossing behavior, but instead exhibit conventional ferromagnetic hysteresis. However, the horizontal shift of the loops remains, indicating that the underlying interfacial coupling persists at lower temperature.

The self-crossing hysteresis loops are not typically observed in standalone (111)LSMO thin films that are the only native magnetic phase deposited on the samples discussed. Such characteristics are commonly attributed to coupled magnetic systems, where two or more interacting magnetic phases give rise to modified net magnetic behavior. The observation of such behavior within the

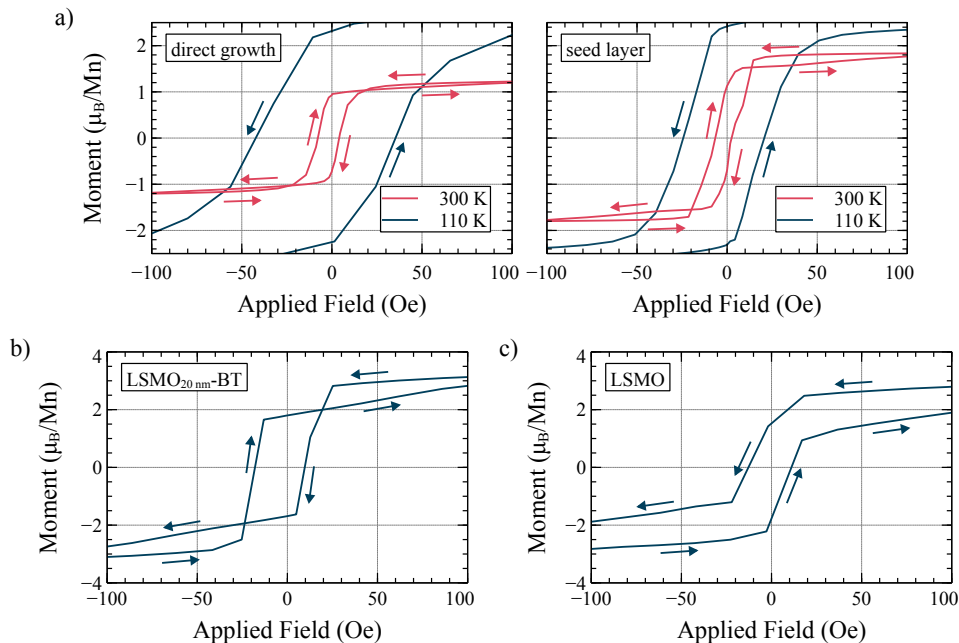


FIG. 5. Zoomed-in hysteresis loops around $H = \pm 100$ Oe. a) LSMO-BT heterostructures with the direct growth (left) and seed layer growth (right). Scans collected at two temperatures are plotted to compare the magnetic response. b) Comparative heterostructure with the thinner LSMO layer. c) Single LSMO layer.

LSMO-BT therefore suggests the possible emergence of an additional magnetic phase beyond the intrinsic ferromagnetism of LSMO.

To elucidate the origin of this anomalous magnetic response, two considerations are addressed. First, the disappearance of self-crossing loops at low temperature may result from the enhanced contribution of the FM LSMO layer to the overall magnetization, effectively masking the coupling effects. This hypothesis can be examined by measuring a similar heterostructure in which the LSMO thickness is substantially reduced, while all other stack components remain unchanged. Second, comparative measurements on a standalone (111)LSMO thin film are required to exclude potential experimental artifacts.

To this end, a comparison is performed with the direct growth LSMO-BT heterostructure having a 20 nm thick LSMO, and with a single LSMO thin film without the BT overlayer. The corresponding hysteresis loops are shown in Figure 5(b,c). Measurements performed on the heterostructure at 110 K (Figure 5(b)) confirm the presence of self-crossing loops. Hysteresis curves collected at other temperatures are appended in the Supporting Information. Notably, the behavior persists at the investigated temperature, as well as lower temperatures down to 2 K, supporting the thickness-dependence hypothesis. A loop shift of -4 Oe is observed along the applied field axis, without a measurable shift along the magnetization axis. The saturation magnetization $T = 110$ K is $3.52 \mu_B/\text{Mn}$. In contrast, the standalone LSMO thin film (Figure 5(c)) exhibits conventional ferromagnetic hys-

teresis loops, with no evidence of self-crossing behavior or horizontal loop shift.

Discussion

Magnetic characterization using PNR, XMCD, and magnetometry consistently indicates that interfacial reconstruction plays a central role in determining the magnetic properties of LSMO-BT heterostructures. In the direct-growth case, the formation of an intermediate interfacial layer coincides with the emergence of a spatially extended magnetic moment beyond the LSMO layer. XAS measurements further suggest that this region is associated with modified manganese oxidation states, consistent with the formation of Mn-based secondary phases driven by interfacial diffusion and chemical reconstruction. In contrast, the introduction of a Te seed layer suppresses the formation of a distinct interfacial phase and reduces structural roughness, while still preserving an extended magnetic profile. The persistence of magnetization beyond the LSMO layer in both growth modes indicates that interfacial reconstruction, rather than purely structural sharpness, governs the magnetic coupling in these systems.

Importantly, the XMCD results do not provide conclusive evidence for a significant magnetic moment on tellurium, suggesting that magnetic proximity effects within the BT layer are not the dominant mechanism responsible for the observed behavior. Instead, the combined

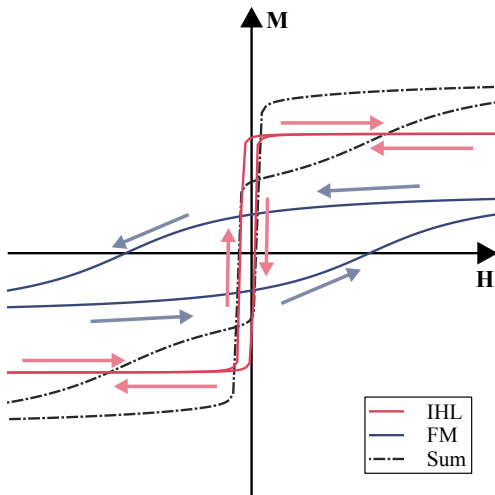


FIG. 6. Deconvoluted model of the self-crossing hysteresis loops observed in LSMO–BT heterostructures. The anomalous self-crossing behavior and magnetization reversal are reproduced by superposing two magnetic contributions: a conventional ferromagnetic (FM) component with lower saturation magnetization and higher coercivity, and an inverted hysteresis loop (IHL) component with higher saturation magnetization and lower coercivity.

data support a scenario in which an emergent manganese-containing interfacial phase contributes an additional magnetic component.

The macroscopic manifestation of this coupling is observed in the form of self-crossing hysteresis loops. These loops can be qualitatively understood as arising from the superposition of two magnetic contributions as schematically deconvoluted in Figure 6: a conventional FM LSMO response and a secondary magnetic phase of lower coercivity and antiparallel alignment, resulting in an inverted hysteresis loop characteristic. Such behavior has been reported in coupled dual-ferromagnetic systems and is consistent with an exchange-spring-like mechanism, in which two magnetic phases with different switching fields are exchange-coupled.

While alternative explanations, including experimental artifacts, must be carefully considered, several observations argue against this possibility: (i) the self-crossing behavior is observed exclusively in heterostructures and not in standalone LSMO films; (ii) the measurements are reproducible across multiple magnetometry platforms, including SQUID and VSM systems; (iii) the applied field range is limited, minimizing remanent field effects; and (iv) the magnetic response systematically depends on heterostructure design [42–46]. Taken together, these results support the intrinsic origin of the observed magnetic behavior.

The precise microscopic structure of the interfacial magnetic phase remains an open question. Possible candidates include manganese oxides and man-

ganese–tellurium compounds such as MnO_2 , Mn_3O_4 , MnTe , or MnTe_2 , all of which can exhibit magnetic ordering [47–50]. Further studies combining atomic-resolution structural characterization with element-specific magnetic probes will be required to fully resolve the nature of this phase. Nevertheless, the present results clearly establish that interfacial chemical reconstruction provides a powerful handle to engineer magnetic coupling in oxide–topological insulator heterostructures.

CONCLUSIONS

In summary, we have demonstrated that magnetic properties of LSMO–BT heterostructures can be controlled through interfacial reconstruction. Direct growth of BT on LSMO leads to the formation of an intermediate manganese-containing interfacial phase, while the introduction of a Te seed layer suppresses this phase and improves interface quality. In both cases, Polarized Neutron Reflectometry reveals a spatially extended magnetic moment beyond the LSMO layer.

The presence of an additional magnetic phase gives rise to unconventional self-crossing hysteresis loops, which we attribute to exchange coupling between the LSMO layer and an emergent interfacial magnetic phase. X-ray absorption spectroscopy indicates that this phase is associated with modified manganese chemistry, while magnetic proximity effects in the BT layer appear to play a secondary role.

These results highlight interfacial chemical reconstruction as a key mechanism for tailoring magnetic coupling in oxide–topological insulator heterostructures. These results position perovskite–chalcogenide heterostructures as a compelling platform for the study and control of emergent interfacial magnetism.

ACKNOWLEDGEMENTS

This project was supported by the Research Council of Norway under Project Number 325063 and the COST Action CA-20116 Network for Innovative and Advanced Epitaxy (OPERA) Short-Term Scientific Mission (STSM). D.B. acknowledges DTU Energy PLD Group (Lyngby, Denmark): Dae-Sung Park, Alessandro Palliotto, Eric Brand, Felix Trier, and Nini Pryds for assistance in film growth and the STSM collaboration; University of Twente (Enschede, the Netherlands), Romar Avila, Emma van der Minne, and Gertjan Koster for assistance in film growth; Gavin Stenning of the Materials Characterisation Laboratory R53 of ISIS (Didcot, UK), as well as Takashi Honda of the High Energy Accelerator Research Organization (Tsukuba, Japan) for their assistance in SQUID/VSM magnetic characterization.

- * ingrid.hallsteinsen@ntnu.no
- [1] K. T. Kang, J. Park, D. Suh, and W. S. Choi, *Advanced Materials* **31**, 1803732 (2019).
 - [2] T. Liu, C. Han, D. Xiang, K. Han, A. Ariando, and W. Chen, *Advanced Science* **7**, 2002393 (2020).
 - [3] Y. Liu, M. Weinert, and L. Li, *Physical Review Letters* **108** (2012), 10.1103/PhysRevLett.108.115501.
 - [4] H. Y. Hwang, Y. Iwasa, M. Kawasaki, B. Keimer, N. Nagao, and Y. Tokura, *Nature materials* **11**, 103 (2012).
 - [5] J. Nitta, T. Akazaki, H. Takayanagi, and T. Enoki, *Physical Review Letters* **78**, 1335 (1997).
 - [6] M. Mogi, M. Kawamura, R. Yoshimi, A. Tsukazaki, Y. Kozuka, N. Shirakawa, K. Takahashi, M. Kawasaki, and Y. Tokura, *Nature materials* **16**, 516 (2017).
 - [7] C.-Z. Chang, J. Zhang, X. Feng, J. Shen, Z. Zhang, M. Guo, K. Li, Y. Ou, P. Wei, L.-L. Wang, *et al.*, *Science* **340**, 167 (2013).
 - [8] F. Katmis, V. Lauter, F. Nogueira, B. Assaf, M. Jamer, P. Wei, B. Satpati, J. Freeland, I. Eremin, D. Heiman, P. Jarillo-Herrero, and J. Moodera, *Nature* **533** (2016), 10.1038/nature17635.
 - [9] M. Li, Q. Song, W. Zhao, J. A. Garlow, T.-H. Liu, L. Wu, Y. Zhu, J. S. Moodera, M. H. W. Chan, G. Chen, and C.-Z. Chang, *Phys. Rev. B* **96**, 201301 (2017).
 - [10] Y. Tokura, K. Yasuda, and A. Tsukazaki, *Nature Reviews Physics* **1**, 126 (2019).
 - [11] J. Checkelsky, R. Yoshimi, A. Tsukazaki, K. Takahashi, Y. Kozuka, J. Falson, M. Kawasaki, and Y. Tokura, *Nature Physics* **10**, 731 (2014).
 - [12] M. Mogi, R. Yoshimi, A. Tsukazaki, K. Yasuda, Y. Kozuka, K. S. Takahashi, M. Kawasaki, and Y. Tokura, *Applied Physics Letters* **107**, 56 (2015).
 - [13] S. Qi, Z. Liu, M. Chang, R. Gao, Y. Han, and Z. Qiao, *Physical Review B* **101**, 241407 (2020).
 - [14] M. M. Otrokov, I. I. Klimovskikh, H. Bentmann, D. Estyunin, A. Zeugner, Z. S. Aliev, S. Gaß, A. Wolter, A. Koroleva, A. M. Shikin, *et al.*, *Nature* **576**, 416 (2019).
 - [15] Y. Gong, J. Guo, J. Li, K. Zhu, M. Liao, X. Liu, Q. Zhang, L. Gu, L. Tang, X. Feng, *et al.*, *Chinese Physics Letters* **36**, 076801 (2019).
 - [16] Y. Deng, Y. Yu, M. Z. Shi, Z. Guo, Z. Xu, J. Wang, X. H. Chen, and Y. Zhang, *Science* **367**, 895 (2020).
 - [17] Q. Li, S.-K. Mo, and M. T. Edmonds, *Nanoscale* **16**, 14247 (2024).
 - [18] L. Alegria, H. Ji, N. Yao, J. Clarke, R. J. Cava, and J. R. Petta, *Applied Physics Letters* **105** (2014), 10.1063/1.4892353.
 - [19] C. Tang, C.-Z. Chang, G. Zhao, Y. Liu, Z. Jiang, C.-X. Liu, M. R. McCartney, D. J. Smith, T. Chen, J. S. Moodera, *et al.*, *Science advances* **3**, e1700307 (2017).
 - [20] S. Zhu, G. Shi, P. Zhao, D. Meng, G. Liang, X. Zhai, Y. Lu, Y. Li, L. Chen, and K. Wu, *Chinese Physics B* **27**, 076801 (2018).
 - [21] S. Zhu, D. Meng, G. Liang, G. Shi, P. Zhao, P. Cheng, Y. Li, X. Zhai, Y. Lu, L. Chen, and K. Wu, *Nanoscale* **10**, 10041 (2018).
 - [22] L. Pan, A. Grutter, P. Zhang, X. Che, T. Nozaki, A. Stern, M. Street, B. Zhang, B. Casas, Q. L. He, *et al.*, *Advanced Materials* **32**, 2001460 (2020).
 - [23] L. Riddiford, A. Grutter, T. Pillsbury, M. Stanley, D. Hickey, P. Li, N. Alem, N. Samarth, and Y. Suzuki, *Physical Review Letters* **128** (2022), 10.1103/PhysRevLett.128.126802.
 - [24] R. Watanabe, R. Yoshimi, M. Kawamura, M. Mogi, A. Tsukazaki, X. Yu, K. Nakajima, K. S. Takahashi, M. Kawasaki, and Y. Tokura, *Applied Physics Letters* **115** (2019), 10.1063/1.5111891.
 - [25] Y. Tokura, *JSAP Int* **2**, 12 (2000).
 - [26] M. Izumi, Y. Ogimoto, Y. Konishi, T. Manako, M. Kawasaki, and Y. Tokura, *Materials Science and Engineering: B* **84**, 53 (2001).
 - [27] T. Kimura, Y. Tomioka, H. Kuwahara, A. Asamitsu, M. Tamura, and Y. Tokura, *Science* **274**, 1698 (1996).
 - [28] L. Berndt, V. Balbarin, and Y. Suzuki, *Applied Physics Letters* **77**, 2903 (2000).
 - [29] J. Lloyd-Hughes, C. Mosley, S. Jones, M. R. Lees, A. Chen, Q. X. Jia, E.-M. Choi, and J. MacManus-Driscoll, *Nano Letters* **17**, 2506 (2017).
 - [30] Y. Chen, J. G. Analytis, J.-H. Chu, Z. Liu, S.-K. Mo, X.-L. Qi, H. Zhang, D. Lu, X. Dai, Z. Fang, *et al.*, *science* **325**, 178 (2009).
 - [31] H. Zhang, C.-X. Liu, X.-L. Qi, X. Dai, Z. Fang, and S.-C. Zhang, *Nature physics* **5**, 438 (2009).
 - [32] G. Koren, *Physical Review B* **97**, 054405 (2018).
 - [33] S. Zhu, G. Shi, P. Zhao, D. Meng, G. Liang, X. Zhai, Y. Lu, Y. Li, L. Chen, and K. Wu, *Chinese Physics B* **27**, 076801 (2018).
 - [34] W. Wang, M. W. Daniels, Z. Liao, Y. Zhao, J. Wang, G. Koster, G. Rijnders, C.-Z. Chang, D. Xiao, and W. Wu, *Nature materials* **18**, 1054 (2019).
 - [35] X. Yang, T. Zhao, Q. Liu, K. Zhao, Z. Wei, and Y. Zhao, *Ceramics International* **46**, 4748 (2020).
 - [36] Q. Lu, P. Li, Z. Guo, G. Dong, B. Peng, X. Zha, T. Min, Z. Zhou, and M. Liu, *Nature communications* **13**, 1650 (2022).
 - [37] Q. Miao, C. Kang, Y. H. Song, and W. Zhang, *Applied Physics Letters* **122** (2023), 10.1063/5.0147158.
 - [38] H. Huang, Q. Liu, and M. Zhang, *Journal of Alloys and Compounds* **976**, 173099 (2024).
 - [39] C. Lichtensteiger, *Journal of Applied Crystallography* **51**, 1745 (2018).
 - [40] J. Kavich, M. Warusawithana, J. Freeland, P. Ryan, X. Zhai, R. Kodama, and J. Eckstein, *Physical Review B—Condensed Matter and Materials Physics* **76**, 014410 (2007).
 - [41] I. Hallsteinsen, M. Moreau, A. Grutter, M. Nord, P.-E. Vullum, D. A. Gilbert, T. Bolstad, J. Grepstad, R. Holmestad, S. Selbach, *et al.*, *Physical Review B* **94**, 201115 (2016).
 - [42] M. O'Shea and A.-L. Al-Sharif, *Journal of Applied Physics* **75**, 6673 (1994).
 - [43] S. Valvidares, L. Alvarez-Prado, J. Martin, and J. Alameda, *Physical Review B* **64**, 134423 (2001).
 - [44] P. Ghising, B. Samantaray, and Z. Hossain, *Physical Review B* **101**, 024408 (2020).
 - [45] R. G. Bhardwaj, A. Kataiiliha, P. C. Lou, W. Beyermann, and S. Kumar, *Journal of Magnetism and Magnetic Materials* **618**, 172886 (2025).
 - [46] G. Wei, H. Gong, L. Bai, H. Wang, Z. Zhou, W. Xie, H. Huang, J. Zou, W. Zhao, Y. Chen, *et al.*, *Physical Review B* **113**, 104424 (2026).
 - [47] L.-T. Tseng, Y. Lu, H. M. Fan, Y. Wang, X. Luo, T. Liu, P. Munroe, S. Li, and J. Yi, *Scientific reports* **5**, 9094 (2015).
 - [48] A. Vázquez-Olmos, R. Redón, G. Rodríguez-Gattorno,

- M. E. Mata-Zamora, F. Morales-Leal, A. L. Fernández-Osorio, and J. M. Saniger, *Journal of colloid and interface science* **291**, 175 (2005).
- [49] R. D. Gonzalez Betancourt, J. Zubac, K. Geishendorf, P. Ritzinger, B. Ruvica, T. Kotte, J. Zelezny, K. Olejnik, G. Springholz, B. Buchner, *et al.*, *npj Spintronics* **2**, 45 (2024).
- [50] W. Chen, J.-m. Zhang, Y.-z. Nie, Q.-l. Xia, and G.-h. Guo, *Journal of Magnetism and Magnetic Materials* **508**, 166878 (2020).

Supporting Information: Tailoring Emergent Magnetic Moment in $\text{La}_{0.7}\text{Sr}_{0.3}\text{MnO}_3\text{-Bi}_2\text{Te}_3$ Heterostructures *via* Interfacial Reconstructions

Damian Brzozowski¹, Yu Liu¹, Øyvind Finnseth¹, Egil Y. Tokle¹, Andrew J. Caruana², Christy J. Kinane², Alexander J. Grutter³, Dennis G. Meier^{1,4}, and Ingrid G. Hallsteinsen¹

¹*Department of Materials Science and Engineering, Norwegian University of Science and Technology, Trondheim, Norway*

²*ISIS Facility, STFC Rutherford Appleton Laboratory, Harwell Science and Innovation Campus, Didcot, Oxfordshire, United Kingdom*

³*NIST Center for Neutron Research, National Institute of Standards and Technology, Gaithersburg, Maryland, United States*

⁴*Faculty of Physics, University of Duisburg-Essen, Germany*

Structural Analysis

Figure 1 shows HRXRD scan of the seed-layer sample. The peak yielding the highest intensity corresponds to the (111)STO substrate, while the (111)LSMO peak is located at $2\theta = 40.45^\circ$. Based on the distance between the lattice fringes of the LSMO film, the thickness of the film is approximately 75 nm.

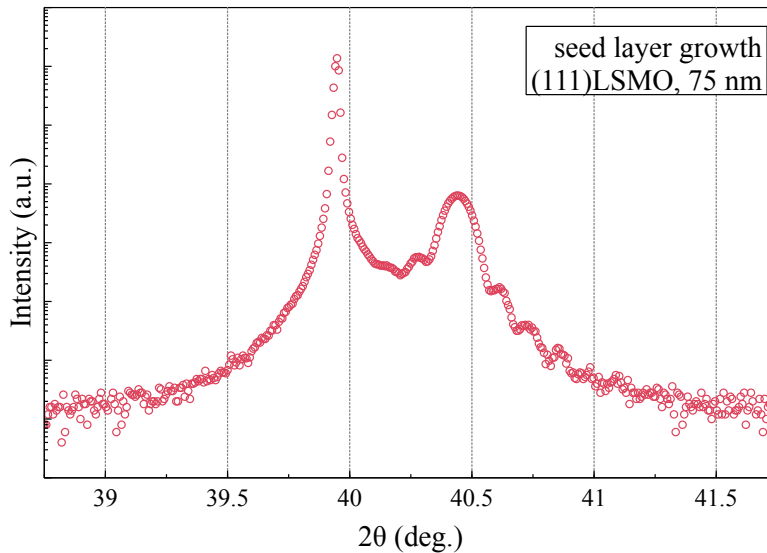


Figure 1: HRXRD of the seed layer heterostructure showing the (111)STO substrate peak and the LSMO peak with the estimated layer thickness of about 75 nm.

Magnetometry Measurements

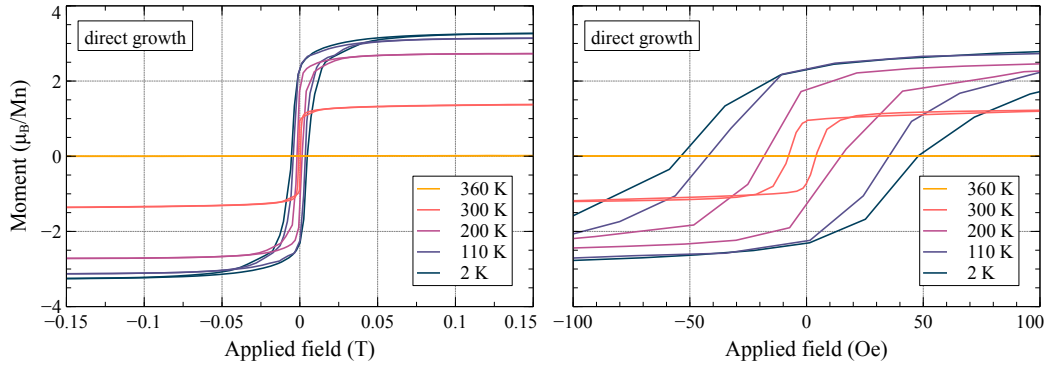


Figure 2: Magnetic hysteresis curves of the direct growth heterostructure collected at a range of temperatures. The right side plot shows a zoomed-in region at applied field $H = \pm 100$ Oe.

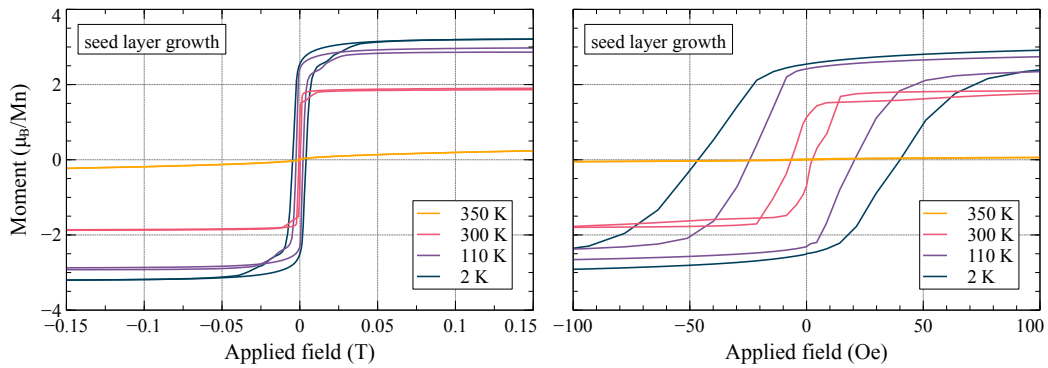


Figure 3: Magnetic hysteresis curves of the seed layer heterostructure collected at a range of temperatures. The right side plot shows a zoomed-in region at applied field $H = \pm 100$ Oe.

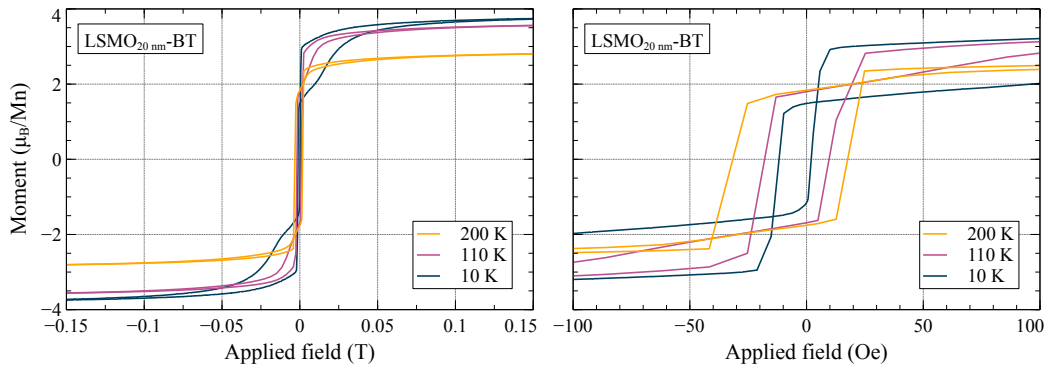


Figure 4: Magnetic hysteresis curves of the heterostructure with thin LSMO layer collected at a range of temperatures. The right side plot shows a zoomed-in region at applied field $H = \pm 100$ Oe.

Polarized Neutron Reflectometry

The process of building the precise model relies on creating the simplest model expected, which serves as a base for further building up of the fitting parameters. It must be noted that the figure of merit χ^2 does not reflect the accuracy to the real state of the stack, but rather how well the collected data is fit. Therefore, in order to create a model that is reasonably accurate, it is critical to collect preliminary data on the modeled systems. For this study, HRXRD was used to estimate the thickness of the layers through the fitting process in InteractiveXRDFit. Raman spectroscopy was used to confirm the correct stoichiometry of Bi_2Te_3 , and bulk magnetometry was used to measure field dependent magnetization in both samples.

In the case of LSMO-BT heterostructures with seeded and direct deposition, the main questions to be answered by PNR are: 1) Does either of deposition approaches lead to observable changes at the interface? 2) Is there a magnetic phase present outside of LSMO?

Model 1 is created to fit the data of the heterostructure with direct deposition. It consists of magnetic LSMO and BT, grown on STO substrate. The starting thickness values are set based on the HRXRD data and equal 79.0 nm and 20.0 nm for LSMO and BT, respectively. Both parameters are set to fit between the range of ± 5 nm. LSMO has a magnetic scattering length density component (ρ_M) initially equal 2.0 and fit between the range of $0.0 \times 10^{-4} \text{ nm}^{-2}$ to $5.0 \times 10^{-4} \text{ nm}^{-2}$. In addition, the roughness of each layer (*interface*) is set as a fitting parameter between 0.0 nm and 10.0 nm. The initial roughness values are equal 2.0 nm for STO, 5.0 nm for LSMO, and 6.0 nm for BT. The scattering length density values (ρ) are taken from the NIST Neutron Activation and Scattering Calculator, and their fitting range is set to $\pm 10\%$.

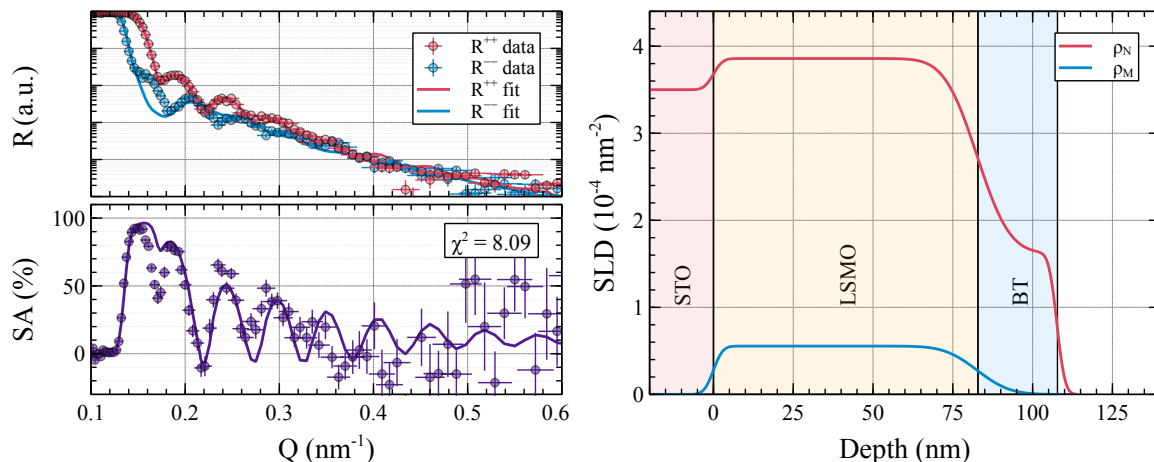


Figure 5: PNR Model 1: basic LSMO and BT stack. Thickness values implemented in the model are based on the HRXRD and XRR data. The LSMO layer is magnetic, while for BT the magnetic fit parameters are fixed to zero. The left panel shows reflectivity data R of both spin channels along with the model fit, as well as the calculated spin asymmetry SA . The right panel shows the suggested SLD and mSLD profiles. The colored areas highlight the layers present in the stack.

The results for Model 1 are summarized in Figure 5. The left panel shows reflectivity data (points) and fit (lines) plotted in the logarithmic scale, as well as the resulting spin asymmetry SA . The right panel shows the SLD and mSLD profiles along with the shaded areas that represent the thickness of the layers predicted by the model. The figure of merit χ^2 reaches 8.09, indicating a poor

match with the data. It is evident from the SA plot that the fit is greatly mismatched at low Q . The values achieved for thickness parameters differ noticeably from the initial values and equal 82.6 nm for LSMO and 25.0 nm for BT. Notably, the value obtained for BT resides at the limit of the fitting range. The mSLD of LSMO is equal $0.55 \times 10^{-4} \text{ nm}^{-2}$. Such large deviation from the initial value may be a result of the temperature at which the measurements were carried out (T 300 K). Finally, the roughness values are 2.3 nm for STO, 8.1 nm for LSMO, and 2.0 nm for BT.

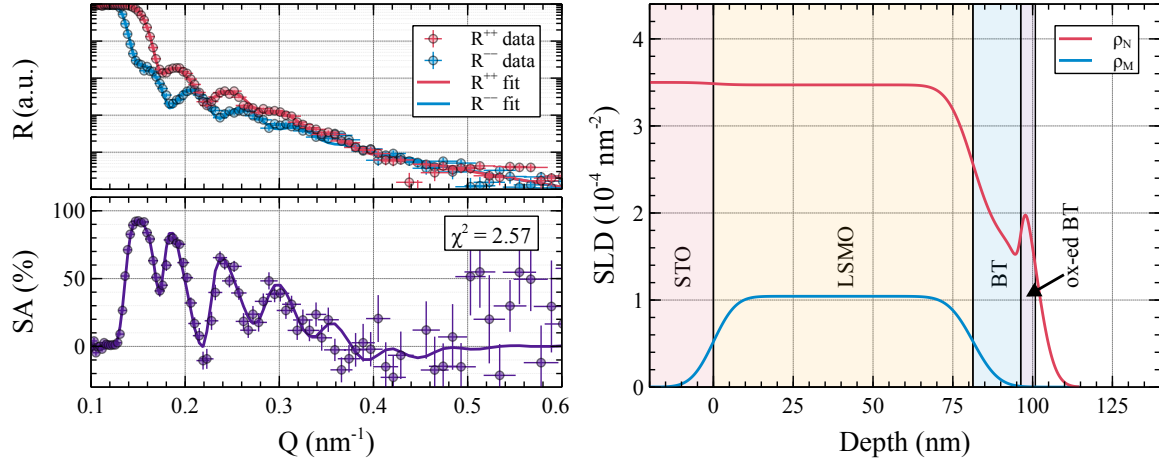


Figure 6: PNR Model 2: LSMO and BT stack with oxidized BT upper layer. Thickness values implemented in the model are based on the HRXRD and XRR data. The LSMO layer is magnetic, while for BT and oxidized BT the magnetic fit parameters are fixed to zero. The left panel shows reflectivity data R of both spin channels along with the model fit, as well as the calculated spin asymmetry SA . The right panel shows the suggested SLD and mSLD profiles. The colored areas highlight the layers present in the stack.

The following Model 2 assumes the presence of the oxidized topmost layer of BT. Oxidation effects are commonly observed in uncapped BT thin films and affect the scattering length density. The density ρ of the oxidized BT is set to $2.5 \times 10^{-4} \text{ nm}^{-2}$ with $\pm 10\%$ fitting range. The thickness is set to 5.0 nm, and the roughness to 1.0 nm. All parameters of the remaining layers remain unchanged. Figure 6 shows the result of Model 2. The fitting is greatly improved and χ^2 reaches 2.57. Notably, the fit appears much more accurate at Q below 0.2 nm^{-1} . The thickness values are 81.4 nm for LSMO, 15.0 nm for BT, and 4.5 nm for oxidized BT. Once again, the model assumes the thickness of BT at the limit of the fitting range. However, the lower limit is preferred with this model iteration. This is expected, considering that the oxidized BT layer is introduced. Together, they form a layer of 19.5 nm, which is in agreement with the HRXRD data. What is more, mSLD of LSMO is considerably different and reaches $1.0 \times 10^{-4} \text{ nm}^{-2}$. Such discrepancy may indicate that there may be additional magnetic component present within the stack.

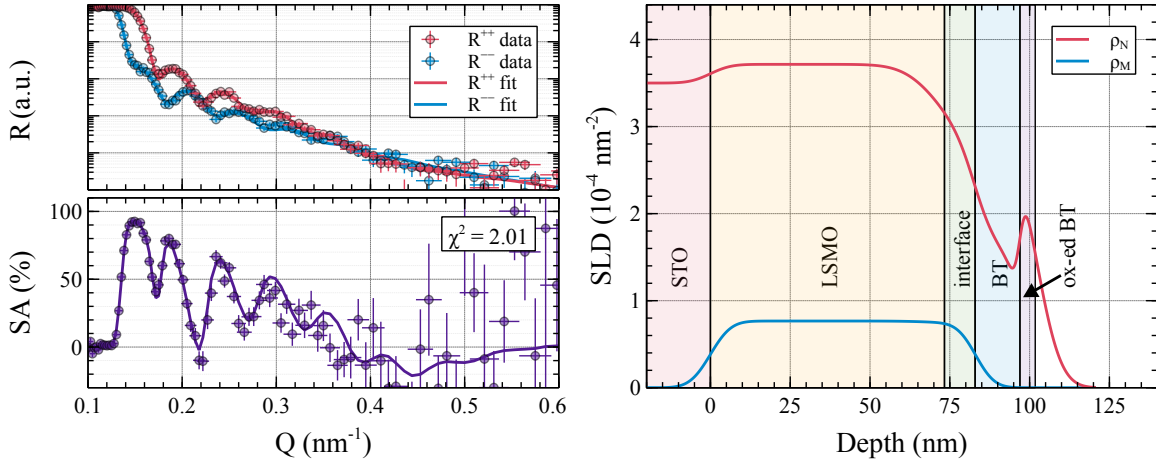


Figure 7: PNR Model 3: including the interfacial phase. The LSMO layer is magnetic, while for the interface, BT, and oxidized BT the magnetic fit parameters are fixed to zero. The left panel shows reflectivity data R of both spin channels along with the model fit, as well as the calculated spin asymmetry SA . The right panel shows the suggested SLD and mSLD profiles. The colored areas highlight the layers present in the stack.

Model 3, shown in Figure 7, adds non-magnetic interfacial layer between LSMO and BT, with the thickness of 5.0 nm fitting between the range from 0.0 nm to 10.0 nm. SLD of the interfacial layer is set to $2.5 \times 10^{-4} \text{ nm}^{-2}$ and the fitting range of $0.5\text{-}3.0 \times 10^{-4} \text{ nm}^{-2}$. With the interfacial layer added, the bottom fitting limit of the BT decreased from 15 nm to 10 nm. The fit is improved and χ^2 reaches 2.01. Thickness values equal 73.2 nm for LSMO, 9.9 nm for the interface, 13.8 nm for BT, and 5.1 nm for oxidized BT. Magnetic scattering length density of LSMO is fit to $0.8 \times 10^{-4} \text{ nm}^{-2}$, once more changing considerably between the models.

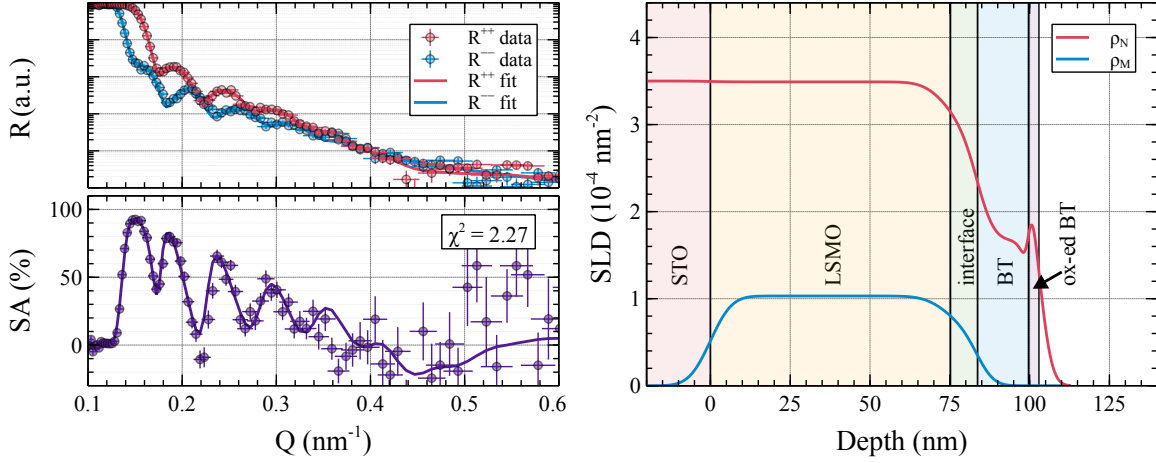


Figure 8: PNR Model 4: magnetic fit parameters of the interfacial phase are set within the model as variables. The LSMO and the interfacial phase layers are magnetic, while for BT and oxidized BT the magnetic fit parameters are fixed to zero. The left panel shows reflectivity data R of both spin channels along with the model fit, as well as the calculated spin asymmetry SA . The right panel shows the suggested SLD and mSLD profiles. The colored areas highlight the layers present in the stack.

Figure 8 summarizes the results of Model 4, in which ρM fit parameter is added to the interfacial layer. The initial ρM value is set to $0.0 \times 10^{-4} \text{ nm}^{-2}$ and the fitting range is 0.0 - $1.0 \times 10^{-4} \text{ nm}^{-2}$. The model results in a marginally poorer fit with $\chi^2 = 2.27$. The SA plot reveals that the fit above $Q = 0.2 \text{ nm}^{-1}$ misses the features observed in the data such as the negative spin asymmetry at $\sim 0.22 \text{ nm}^{-1}$. Notably, ρM of the interfacial layer has the value of $0.59 \times 10^{-4} \text{ nm}^{-2}$.

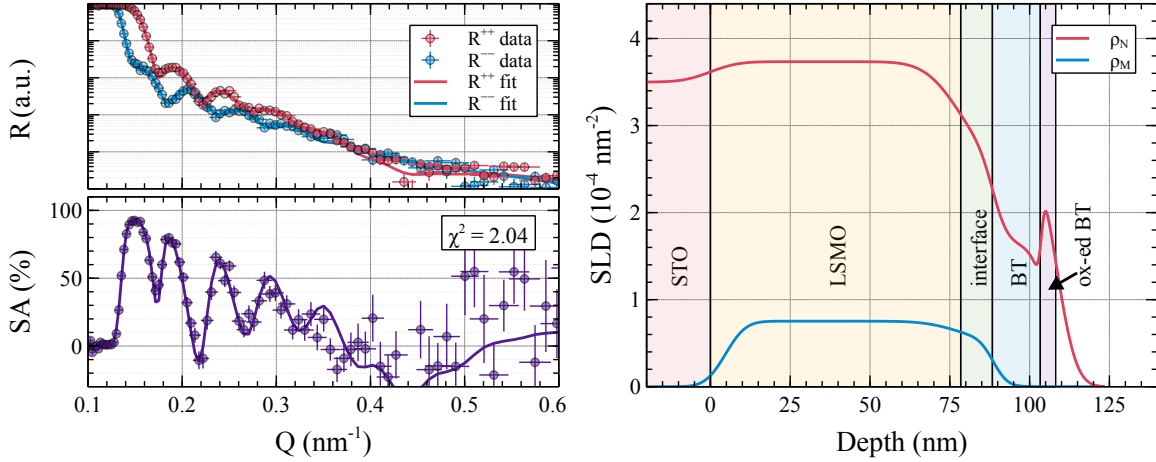


Figure 9: PNR Model 5: based on Model 4, where an additional fit parameter is added for the LSMO layer to account for magnetic dead layer between LSMO and STO. The LSMO and the interfacial phase layers are magnetic, while for BT and oxidized BT the magnetic fit parameters are fixed to zero. The left panel shows reflectivity data R of both spin channels along with the model fit, as well as the calculated spin asymmetry SA . The right panel shows the suggested SLD and mSLD profiles. The colored areas highlight the layers present in the stack.

Model 5 shown in Figure 9 adds LSMO magnetic dead layer to fit parameters. The dead layer is set between STO and LSMO. The remaining parameters remain as in the previous model. χ^2 is improved relative to that of Model 4 and equals 2.04. Once again, the interfacial layer yields non-zero $\rho_M = 0.50 \times 10^{-4} \text{ nm}^{-2}$. Importantly, this model fits the negative spin asymmetry at $Q = 0.22 \text{ nm}^{-1}$ more closely. The following Model 6 is presented in the main text. It adds the topmost surface layer to account for surface contamination, and yields the best fit with $\chi^2 = 1.69$.

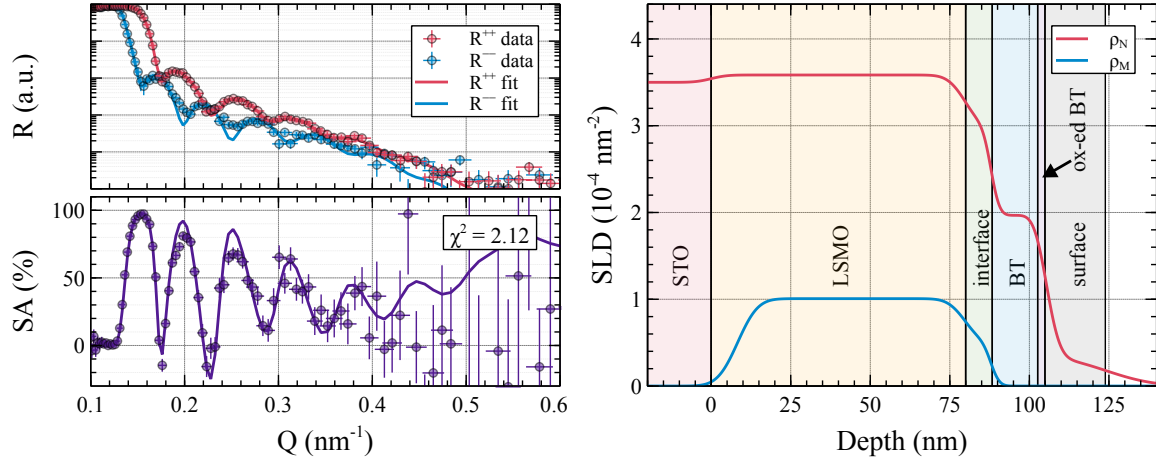


Figure 10: PNR Model 7: Model 6 applied to the data of sample S4. The LSMO and the interfacial phase layers are magnetic, while for the remaining layers the magnetic fit parameters are fixed to zero. The left panel shows reflectivity data R of both spin channels along with the model fit, as well as the calculated spin asymmetry SA . The right panel shows the suggested SLD and mSLD profiles. The colored areas highlight the layers present in the stack.

The following models are applied to the second sample grown with the intermediate tellurium seed layer between LSMO and BT. Firstly, Model 7 is built based on Model 6 of the previous sample. Here, initial thickness parameters are changed to match the results obtained from the HRXRD data for the second sample. The remaining parameters remain the same. χ^2 of Model 7 presented in Figure 10 equals 2.12. It is evident from the reflectivity R and spin asymmetry SA plots that the model misses the features at Q above 0.8 nm^{-1} , and that the R^{--} data is not well represented within the model. Similar to the first sample, the seed layer sample model results in non-zero ρ_M at the interface. In addition, SLD of the BT layer is better-defined, indicative of improved layer roughness.

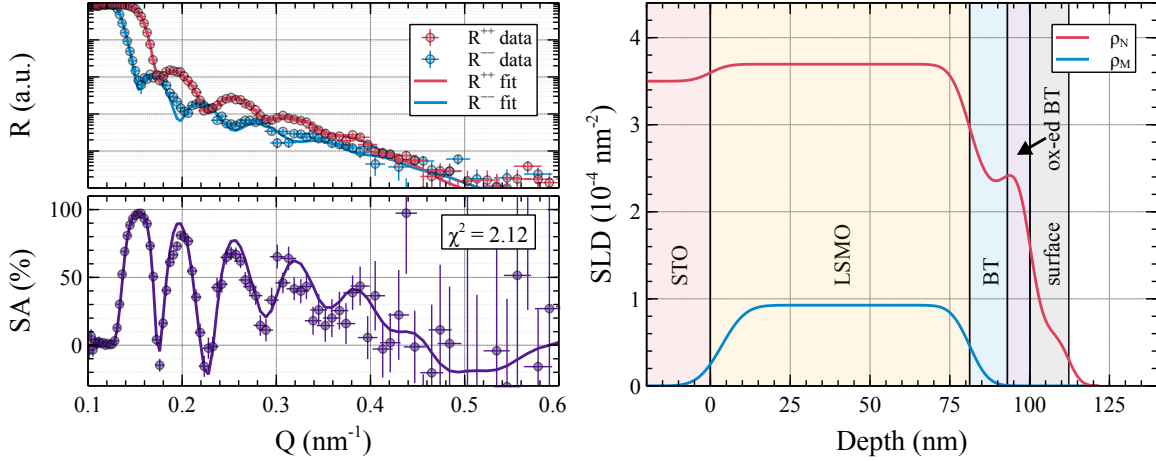


Figure 11: PNR Model 8: based on Model 7, with the interfacial layer removed. The LSMO layer is magnetic, while for the remaining layers the magnetic fit parameters are fixed to zero. The left panel shows reflectivity data R of both spin channels along with the model fit, as well as the calculated spin asymmetry SA . The right panel shows the suggested SLD and mSLD profiles. The colored areas highlight the layers present in the stack.

One of the questions to be answered with the PNR analysis is whether the different deposition protocol affects the interface between LSMO and BT. To this end, two following models explore changed conditions between the layers. Model 8 shown in Figure 11 removes the intermediate interfacial layer. The resulting fit gives $\chi^2 = 2.12$ —the same as that of Model 7. Model 9 shown in Figure 12 exchanges the interfacial layer for a separate thin tellurium layer. The initial thickness value is set to 2 nm and ranged between 0-3 nm. The final fit result approximates the thickness of Te to 0.13 nm, and the figure of merit $\chi^2 = 2.53$, indicative of a worse match to the data than two previous models.

A magnetic component ρ_{hoM} is added to the tellurium layer in Model 10 presented in Figure 13. The fitting range is set to $0.00-1.00 \times 10^{-4} \text{ nm}^{-2}$, and the final result assumes $\rho_{hoM} = 0.03 \times 10^{-4} \text{ nm}^{-2}$. Once again, the figure of merit χ^2 indicates that the model is not improved. Considering that both models introducing the tellurium layer do not improve the fit, we explore the approach that eliminates intermediate layers between LSMO and BT. The final fit for this dataset is shown in the main text and is based on Model 8, where the LSMO layer is split into two sub-layers.

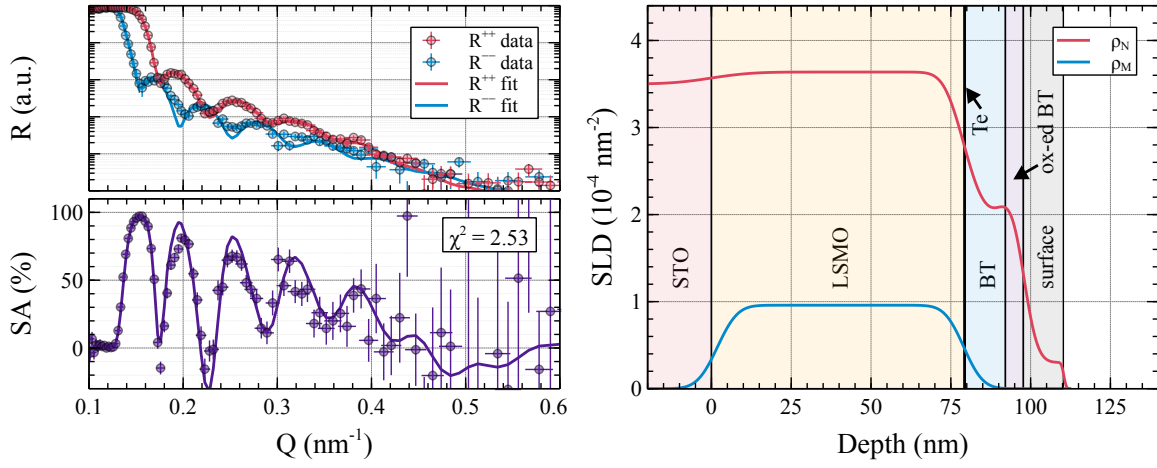


Figure 12: PNR Model 9: based on Model 8, where an intermediate tellurium layer is introduced between LSMO and BT. The LSMO layer is magnetic, while for the remaining layers the magnetic fit parameters are fixed to zero. The left panel shows reflectivity data R of both spin channels along with the model fit, as well as the calculated spin asymmetry SA . The right panel shows the suggested SLD and mSLD profiles. The colored areas highlight the layers present in the stack.

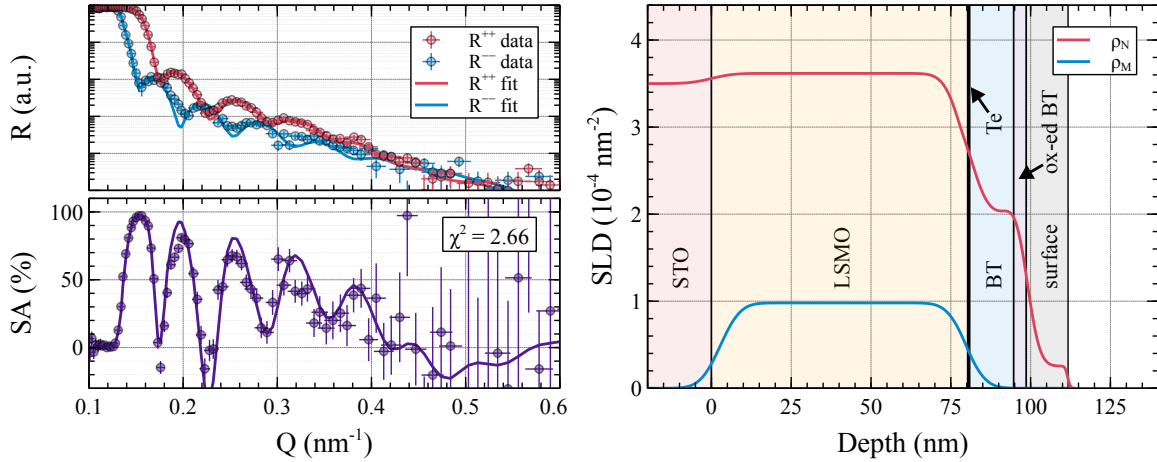


Figure 13: PNR Model 10: based on Model 9, where the tellurium layer has its magnetic fit parameters set as variables. The left panel shows reflectivity data R of both spin channels along with the model fit, as well as the calculated spin asymmetry SA . The right panel shows the suggested SLD and mSLD profiles. The colored areas highlight the layers present in the stack.